14 Feb 2024

Mesoporous RE0.5Ce0.5O2-X Fluorite Electrocatalysts For The Oxygen Evolution Reaction

Sreya Paladugu

Ibrahim Munkaila Abdullahi

Harish Singh

Sam Spinuzzi

et. al. For a complete list of authors, see https://scholarsmine.mst.edu/chem_facwork/3677

Recommended Citation

S. Paladugu et al., "Mesoporous RE0.5Ce0.5O2-X Fluorite Electrocatalysts For The Oxygen Evolution Reaction," *ACS Applied Materials and Interfaces*, vol. 16, no. 6, pp. 7014 - 7025, American Chemical Society, Feb 2024.
The definitive version is available at https://doi.org/10.1021/acsami.3c14977

ACS APPLIED MATERIALS & INTERFACES

www.acsami.org

Research Article

Mesoporous $RE_{0.5}Ce_{0.5}O_{2-x}$ Fluorite Electrocatalysts for the Oxygen Evolution Reaction

Sreya Paladugu, Ibrahim Munkaila Abdullahi, Harish Singh, Sam Spinuzzi, Manashi Nath, and Katharine Page*

Cite This: *ACS Appl. Mater. Interfaces* 2024, 16, 7014–7025

Read Online

ACCESS | Metrics & More | Article Recommendations | Supporting Information

ABSTRACT: Developing highly active and stable electrocatalysts for the oxygen evolution reaction (OER) is key to improving the efficiency and practical application of various sustainable energy technologies including water electrolysis, CO_2 reduction, and metal air batteries. Here, we use evaporation-induced self-assembly (EISA) to synthesize highly porous fluorite nanocatalysts with a high surface area. In this study, we demonstrate that a 50% rare-earth cation substitution for Ce in the CeO_2 fluorite lattice improves the OER activity and stability by introducing oxygen vacancies into the host lattice, which results in a decrease in the adsorption energy of the OH* intermediate in the OER. Among the binary fluorite compositions investigated, $Nd_2Ce_2O_7$ is shown to display the lowest OER overpotential of 243 mV, achieved at a current density of 10 mA cm^{-2}, and excellent cycling stability in an alkaline medium. Importantly, we demonstrate that rare-earth oxide OER electrocatalysts with high activity and stability can be achieved using the EISA synthesis route without the incorporation of transition and noble metals.

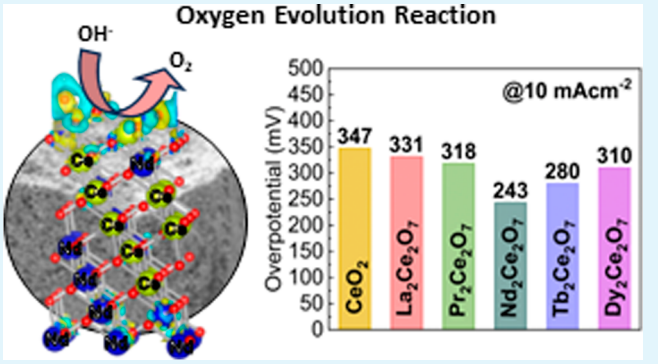

KEYWORDS: *electrocatalyst, OER, fluorites, rare earth cations, mesoporous, oxygen vacancies, high entropy oxides*

INTRODUCTION

There is an urgent need to develop large-scale sustainable energy solutions that reduce our reliance on fossil fuels and mitigate the effects of climate change on our society. The oxygen evolution reaction (OER), which involves the oxidation of water to oxygen, is a fundamental half-reaction involved in various electrochemistry-based sustainable energy technologies including water electrolysis, the CO_2 reduction reaction, fuel cells, and metal air batteries.[1−4] The overall energy efficiency of these technologies is significantly limited by the sluggish reaction kinetics of the OER; thus, the large-scale industrial applicability of these technologies relies on the development of highly active and stable electrochemical catalysts for the OER.

OER catalysts with the highest reported activity thus far consist primarily of precious metals and their oxides (Ru, Ir, RuO_2, and IrO_2).[5] However, the large-scale adoption of these precious-metal-based catalysts is limited by their poor durability in alkaline media, scarcity, and high cost, motivating the search for alternative, precious metal-free catalysts. Ceria, CeO_2, is naturally abundant and corrosion-resistant in an alkaline environment, allowing it to function as a stable electrocatalyst.[2,6] While pure CeO_2 does not exhibit high activity for the OER, numerous studies have shown that the catalytic performance of CeO_2 for the OER can be significantly enhanced by doping or substituting elements into the host fluorite structure to enhance the concentration of oxygen defects.[1,2,6−8] In the case of the OER catalysts, oxygen vacancies have been demonstrated to enhance activity by providing catalytically active sites and modifying adsorption energy, thus promoting reaction intermediate adsorption. This is achieved through adjustments in the local electron density distribution near the defects and a reduction in mass transfer resistance.[1,4,6,7,9,10] Thus far, ceria has been investigated as a cocatalyst or support for the OER, in combination with transition metals or noble metals.[1,2,7,8] However, ceria-based mixed oxides containing rare earth (RE) elements in place of transition or noble metal cations remain unexplored for the OER.[1]

The present work seeks to enhance the intrinsic catalytic activity of CeO_2 for the OER by substituting a single RE cation into its crystal structure, thereby modifying the concentration of oxygen vacancies and the consequential metal−oxygen

Received: October 7, 2023
Revised: January 2, 2024
Accepted: January 3, 2024
Published: February 3, 2024

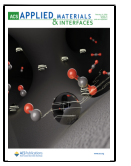

https://doi.org/10.1021/acsami.3c14977
ACS Appl. Mater. Interfaces 2024, 16, 7014−7025

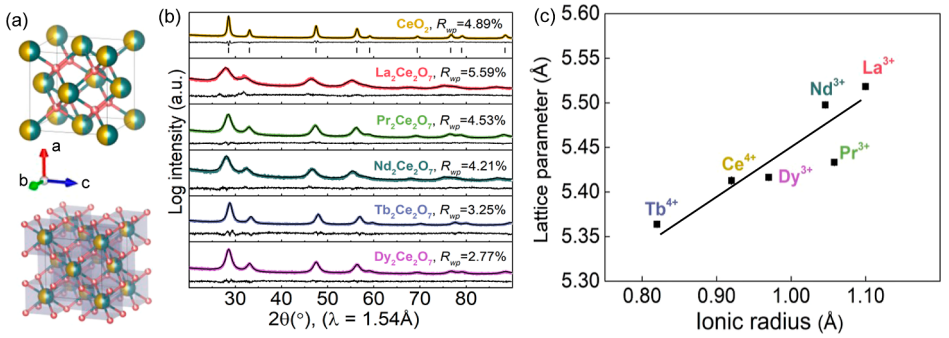

Figure 1. (a) Salient features of the $RE_{0.5}M_{0.5}O_{2-x}$ RE fluorite oxide structure family. When the 4+ fluorite metal M site is substituted with mainly trivalent RE (3+) species, charge compensation occurs through point defects on the oxygen sublattice. The unit cell on the top depicts a system where cation sites are occupied, on average, with equal parts of an RE ion and a Ce ion. The defect fluorite can be written as $RE_{0.5}Ce_{0.5}O_{2-x}$. In the unit cell at the bottom, the VIII-fold cation coordination polyhedra are depicted as light purple cubes with the O atoms at the vertices. (b) Rietveld refinements of X-ray powder diffraction data of the fluorite samples. Measured data are shown as colored circles, structure model fits are shown as a black line through the data, and the difference curves in black fall below the data and fits. CeO_2 was refined using a cubic fluorite structure, as indicated by the *hkl* tick marks in black. The binary fluorites in the series were refined using a defect fluorite structure (with 50% RE and 50% Ce on each M site and 7/8ths of the O sites occupied). (c) Variation in lattice parameters from Rietveld refinements of the binary fluorite samples as a function of the ionic radius of the $RE^{3+/4+}$ cations in assumed VII-fold coordination with oxygen.

binding interactions. CeO_2 has a fluorite type crystal structure, and cerium atoms can dynamically and reversibly convert between 4+ and 3+ oxidation states, enabling the formation of oxygen vacancies and a defect rich structure.[11−13] Partial substitution of Ce^{4+} with (mainly) trivalent RE cations can introduce oxygen vacancies into the lattice, reduce/potentially eliminate the need for (much more expensive) noble metal cations, and potentially promote the adsorption of oxygen-containing intermediates due to an increased concentration of oxygen vacancies.[1,14] While RE elements have similar redox properties to transition metals, they have the potential to show unique electrocatalytic properties due to their partially filled 4f orbitals.[15,16] As shown in Figure 1a, when RE cations are introduced into the cubic fluorite lattice, the $Ce^{3+/4+}$ and RE^{3+} cations randomly occupy the 4*a* Wyckoff position, while the oxygen anions occupy the tetrahedral sites on position 8*c*. If there is a 50/50 balance between 3+ and 4+ cations, the oxygen positions are, on average, 7/8ths occupied; such a "defect fluorite" system readily accommodates small increases or decreases in oxygen occupancy, the development of Frenkel defects, and other charge compensating mechanisms. Doping CeO_2 with RE^{3+} cations is known to depress the concentration of Ce^{3+} and introduce large amounts of oxygen vacancies, resulting in a stable defect-rich fluorite structure.[11,12]

While tuning the oxygen defect structure and participating ionic radii in electrocatalysts serve as fundamental approaches to enhancing the intrinsic activity and improving stability, catalytic activity can also be significantly influenced by morphology. Here, we use a soft templating evaporation-induced self-assembly (EISA) approach to synthesize OER fluorite catalysts with a high surface area (SA), porosity, and a nanoarchitecture with the objectives of increasing the number of exposed active sites and improving mass diffusion kinetics.[1,17,18] Wet chemistry-based synthesis methods such as EISA allow for intimate mixing of cations prior to calcination and can be used to achieve target phases at lower temperatures relative to solid state methods due to increased diffusion kinetics of the cations in solution.[19] The lower calcination temperature associated with EISA also facilitates the synthesis of nanosized particles, which exhibit much larger total exposed SAs than their bulk counterparts and an increased number of catalytically active sites. Additionally, surface accessible porosity, which can be engineered using EISA, can improve the diffusion rates of reactants to and products from active sites.[17,18] These effects are well-known to improve the overall efficiency by achieving higher current densities at low overpotentials in the OER.[18] Furthermore, EISA is an inexpensive, highly tunable, and easily scalable synthesis approach, making it feasible for industrial manufacturing.

Fluorite samples with the target compositions CeO_2, $La_2Ce_2O_7$, $Pr_2Ce_2O_7$, $Nd_2Ce_2O_7$, $Tb_2Ce_2O_7$, and $Dy_2Ce_2O_7$ were synthesized using EISA to explore the role of RE cation substitution on the OER activity of fluorite nano-electrocatalysts. We note that we do not control the oxygen stoichiometry in the synthesis route, and thus the family may be more generally described as $RE_{0.5}Ce_{0.5}O_{2-x}$ compositions. The phase purity, crystallinity, and morphology of the samples are investigated using X-ray diffraction (XRD), Brunauer−Emmett−Teller (BET) analysis, and scanning electron microscopy (SEM). Their electrocatalytic activity and stability for the OER are examined in a 1 M KOH electrolyte, exploring their promise for practical application in water splitting or other technologies involving the OER.

EXPERIMENTAL SECTION

Chemicals. Praseodymium(III) nitrate pentahydrate (99.9%), cerium(III) nitrate hexahydrate (99.5%), terbium(III) nitrate hydrate (99.9%), lanthanum(III) nitrate hexahydrate (98%), dysprosium(III) nitrate pentahydrate (99.9%), neodymium(III) nitrate hexahydrate (99.9%), and ethanol (99.5%) were purchased from Thermo Fisher Scientific. Pluronic P123 [a symmetric triblock copolymer comprising poly(ethylene oxide) (PEO) and poly(propylene oxide) (PPO) in an alternating linear fashion] was purchased from Sigma-Aldrich. The metal content of all metal nitrate hydrates was determined immediately upon receipt from the manufacturer and used to prepare sealed aqueous stock solutions.

Carbon cloth (CC) materials for the battery, fuel cell, and supercapacitor were purchased from MSE supplies (Tucson, AZ). Nafion (5 wt %) and isopropanol (*i*Pr-OH) were purchased from Sigma-Aldrich Chemical Reagent Co., Ltd. (St. Louis, MO), and potassium hydroxide (KOH) was purchased from Fisher Scientific (Pittsburgh, USA). All of the reagents were used as received. The deionized (D.I.) water purified through a Millipore system was used

https://doi.org/10.1021/acsami.3c14977
ACS Appl. Mater. Interfaces 2024, 16, 7014−7025

in all experiments. The CC was washed with *i*Pr-OH and D.I. water several times to ensure a clean surface.

Synthesis of Porous Binary Fluorites via a Soft-Templating Method. Porous fluorite compositions were synthesized using a soft templating approach via EISA adapted based on previously reported studies.[20] Briefly, metal nitrate precursor solutions were dissolved in ethanol, under continuous stirring, using Pluronic P123 as a block copolymer template. The solutions were allowed to evaporate in a Petri dish at room temperature for 48 h, and each resulting gel was calcined in air at 600 °C for 4 h in an oven. The following compositions were chosen to investigate the role of RE cation substitution on the electrochemical OER performance of fluorites: $La_2Ce_2O_7$, $Pr_2Ce_2O_7$, $Nd_2Ce_2O_7$, $Tb_2Ce_2O_7$, and $Dy_2Ce_2O_7$. Additionally, the parent CeO_2 was synthesized by using the same method as a reference.

Fabrication of the Working Electrode for the OER. All CC substrates were *i*Pr-OH cleaned, dried, and covered with Teflon tape, leaving an exposed geometric area of 0.283 cm^2. Catalyst ink was prepared by dispersing 10.0 mg of the catalyst in 1.0 mL of 0.8% Nafion in *i*Pr-OH and ultrasonicating for 30 min. A 20 μL ink volume was pipetted out, drop-casted on the CC substrate exposed geometric area, dried at room temperature, and finally heated at 130 °C in an oven for 30 min in air.

Characterization of the Structure and Morphology. Phase identification of the fluorite powder samples was performed by using a Panalytical Empyrean laboratory powder XRD instrument and Cu Kα radiation (λ = 1.5418 Å). Rietveld refinements were performed on the XRD data using the TOPAS v6 software.[21] Data were fit to cubic fluorite and defect fluorite unit cell models with the scale factor, lattice parameter *a*, separate isotropic atomic displacement parameters U_{iso} for O and for cations (constrained to be equivalent for Ce and RE), and Scherrer particle size *L* refined. The particle morphologies of the powder samples were examined using a Zeiss Auriga scanning electron microscope, and the chemical homogeneity of the samples was determined by performing energy-dispersive mapping measurements on pressed pellets of the samples using a Zeiss EVO scanning electron microscope equipped with energy-dispersive X-ray spectroscopy.

The Brunauer−Emmett−Teller (BET) specific SA measurements were performed by loading 100−150 mg of the powder sample in a quartz tube and outgassing overnight at 200 °C under vacuum. The SA of the outgassed samples was then measured by using a Micromeritics Gemini VII surface area analyzer.

The elemental compositions of the fluorite samples were investigated by performing energy-dispersive X-ray fluorescence (EDXRF) measurements on pressed pellets using a Malvern Panalytical Epsilon 1 EDXRF instrument with a Cu Kα source.

The oxidation states present in the samples were determined by performing X-ray photoelectron spectroscopy (XPS) measurements using a KRATOS AXIS 165 X-ray photoelectron spectrometer (Kratos Analytical Limited, Manchester, United Kingdom) with a monochromatic Al X-ray source. The C 1s signal at 284.5 eV was used as a reference to correct for all the XPS binding energies. All XPS spectra were collected from pristine catalyst surfaces without sputtering.

OER Catalytic Performance. Electrochemical measurements were performed using a conventional three-electrode system connected to an IviumStat potentiostat, where the catalyst was used as the working electrode and a graphite rod and a Ag/AgCl electrode were used as counter and reference electrodes, respectively, to measure the electrocatalytic performances. Linear sweep voltammetry (LSV) and cyclic voltammetry (CV) were used to study the OER catalytic performance and cycling stability. All activity data were *iR*-corrected and measured through electrochemical impedance studies to reduce uncompensated solution resistance. All electrolytes were saturated by N_2 (for the OER) bubbles before and during the experiments.

The steady-state performance and durability of all the electrocatalysts in the OER for long-term chronoamperometric stability in the alkaline electrolyte of 1 M KOH solution were carried out in two forms: (i) at a constant current density of 10 mA cm^{-2} for 16 h for all the binary fluorite series and (ii) at various current densities between 5 and 15 mA cm^{-2} as a multistep study, carried out for $Nd_2Ce_2O_7$ and $Dy_2Ce_2O_7$ in a N_2-saturated 1.0 M KOH electrolyte at room temperature.

All potentials measured were calibrated to the reversible hydrogen electrode (RHE) using eq 1

$$E_{(RHE)} = E_{(Ag/AgCl)} + 0.197\ V + 0.059 \times pH \quad (1)$$

All electrolytes were saturated with oxygen (for the OER) bubbles before and during the experiments.

The steady-state performance and durability of all the electrocatalysts in the OER for long-term chronoamperometric stability in an alkaline electrolyte of 1 M KOH solution were characterized in two forms: (a) at a constant current density of 20 mA cm^{-2} for 16 h and (b) at various current densities between 5 and 30 mA cm^{-2} as a multistep study, in N_2-saturated 1.0 M KOH at room temperature.

The Tafel slope, an important parameter to explain the electrokinetic activity of the catalysts for the hydrogen evolution reaction and the OER processes, was estimated from the Tafel plot. The Tafel equation is given as the dependence of overpotential η on the current density *j* as shown in eq 2.

$$\eta = \alpha + \frac{2.3RT}{\alpha nF}\log j \quad (2)$$

where α is the transfer coefficient, *n* is the number of electrons involved in the reaction, and *F* is the Faraday constant. The Tafel slope is given by $\frac{2.3RT}{\alpha nF}$. The Tafel plots in this work were calculated from the reverse scan of CV collected at a scan rate of 2 mV s^{-1} in a nonstirred N_2-saturated 1.0 M KOH solution.

The electrochemical impedance spectroscopy (EIS) experiments were performed within the 10^5 to 10^{-2} Hz frequency range at an AC signal amplitude of 10 mV to study the electrode kinetics and estimate the electrolyte resistance (R_s) and charge transfer resistance at the electrode (catalyst)−electrolyte interface (R_{ct}). The Nyquist plots were collected in N_2-saturated 1.0 M KOH at an applied potential of 0.45 V vs AglAgCl (KCl saturated). The turnover frequency (TOF), mass activity, electrochemically active SA (ECSA), and roughness factor (RF) of the electrocatalysts were calculated using eqs 3−7, respectively.

The TOF for the electrocatalysts was calculated from eq 3

$$TOF = \frac{j \times A}{4 \times m \times F} \quad (3)$$

where *j* is the current density in mA cm^{-2} at a given overpotential (e.g., η = 0.31 V), *A* is the SA of the electrode (0.283 cm^2), *F* is the Faraday constant with a value of 96,485 C mol^{-1}, and *m* is the moles of the catalyst on the electrode.

Mass activity (A g^{-1}) is the current density per unit mass of the active catalyst at a given overpotential. This is calculated from the catalyst loading *m* and the measured current density *j* (mA cm^{-2}) of the catalyst, at η = 0.31 V, as calculated from eq 4.

$$\text{Mass activity} = \frac{j}{m} \quad (4)$$

The ECSA of the catalyst was estimated by measuring the electrochemical double-layer capacitance (C_{DL}) at different scan rates in the non-Faradaic region. It was assumed that the current obtained in the non-Faradaic region is caused by double-layer charging instead of electrochemical reactions or charge transfer. The double-layer current (i_{DL}) was obtained by measuring cyclic voltammograms with various scan rates in a nonstirred N_2-saturated 1.0 M KOH solution. The ratio of the double-layer current (i_{DL}) and the scan rate (v) of CV yielded the specific electrochemical double-layer capacitance (C_{DL}) = average of the absolute values of cathodic and anodic slopes obtained from the CV plot in the non-Faradaic region as described in Figure S5.

$$i_{DL} = C_{DL} \times v \quad (5)$$

https://doi.org/10.1021/acsami.3c14977
ACS Appl. Mater. Interfaces 2024, 16, 7014−7025

Table 1. Lattice Parameter a, Isotropic Atomic Displacement Parameters U_{iso}s, Average Crystalline Correlation Length L, and the Goodness of Fit R_{wp} Resulting from XRD Rietveld Refinements of the Fluorite Sample Series Data[a]

	CeO_2	$La_2Ce_2O_7$	$Pr_2Ce_2O_7$	$Nd_2Ce_2O_7$	$Tb_2Ce_2O_7$	$Dy_2Ce_2O_7$
a (Å)	5.41300(6)	5.5180(6)	5.4330(2)	5.4980(4)	5.3640(2)	5.4160(3)U
U_{iso}(Ce/RE) (Å^2)	0.013	0.0013(3)	0.0025(1)	0.0029(1)	0.0085(1)	0.0168(1)
U_{iso}(O) (Å^2)	0.013	0.0469(1)	0.0125(8)	0.035(1)	0.0113(1)	0.0325(9)
L (nm)	18.89(2)	3.48(1)	5.88(1)	4.64(1)	7.75(1)	6.67(1)
R_{wp}	4.89	5.51	4.53	4.21	3.25	2.77
BET SA (m^2 g^{-1})	122.44	52.11	87.67	60.92	78.61	69.78

[a]Measured BET SA is also shown for the samples.

The ECSA of the catalyst was calculated using eq 6, where C_s is the specific capacitance as reported in an alkaline solution to be between 0.022 and 0.130 mF cm^{-2}.[22] In this study, we assumed the value of

$$C_s = 30\ \mu\text{F cm}^{-2} \quad (6)$$

based on previously reported OER catalysts in an alkaline medium.[22,23]

$$\text{ECSA} = C_{DL}/C_s \quad (7)$$

The RF is another important parameter that defines catalyst surface roughness and can influence the observed catalytic properties. The RF is estimated as the ratio of the ECSA and the geometric electrode area of 0.283 cm^2.

$$\text{RF} = \text{ECSA/SA} \quad (8)$$

Density Functional Theory. Density functional theory (DFT) calculations were performed using the Vienna ab initio simulation package (VASP). To determine the electron exchange−correlation, the generalized gradient approximation was applied to the Perdew−Burke−Ernzerhof (PBE) function scheme. The plane-wave basis set's kinetic cutoff energy was set at 520 eV. The lattice vectors and all atomic positions were optimized by the conjugate gradient algorithm. Geometries were refined until the threshold force was smaller than 0.01 eV/Å and the total energy change was less than 1×10^{-5} eV. The slab models have used the (1 0 0) surface of $Nd_2Ce_2O_7$ and CeO_2, and a 10 Å vacuum in the c-direction was added to avoid periodic boundary interaction. A Monkhorst−Pack scheme K-point grid was set to $9 \times 9 \times 1$ during surface relaxation.

RESULTS AND DISCUSSION

Defect Structure and Sample Morphology. As seen in Figure 1b, Rietveld refinements were performed on powder XRD data to determine the average crystal structure and phase purity of the fluorite samples prepared by calcination at 600 °C. XRD patterns of all samples display broad peaks, indicative of the highly nanocrystalline nature of samples produced using the low-temperature EISA synthesis route. Interestingly, the incorporation of RE^{3+} cations in CeO_2 leads to a clear broadening of diffraction peaks, suggesting a decrease in crystallinity or particle size.

Rietveld refinement of the CeO_2 sample was performed successfully using the canonical ceria fluorite unit cell model described with the space group (S.G.) $Fm\bar{3}m$, where the Ce cations occupy the face-centered Wyckoff position 4a and oxygen anions occupy the tetrahedral 8c position.[13,24] All fluorite samples containing RE cations display a single phase defect fluorite structure, as shown in Figure 1a, also indexed to the S.G. $Fm\bar{3}m$, but with RE^{3+} randomly occupying half the 4a sites and oxygen anions occupying an assumed 7/8ths of 8c sites. The addition of RE^{3+} cations to ceria suppresses the formation of Ce^{3+} and promotes the formation of oxygen vacancies due to the need for charge compensation.[11]

Extracted parameters from Rietveld refinement provide further structural insights into the effects of RE cation incorporation in CeO_2. In an ideal fluorite structure, Ce^{4+} cations are VIII-fold coordinated with oxygen; however, introducing (mainly) RE^{3+} cations into the fluorite lattice results in a change in the average cation coordination from VIII-fold to VII-fold. The ionic radii for VII-fold coordination can be estimated as an average of ionic radii for VI- and VIII-fold coordination. As seen in Table 1 and Figure 1c, inclusion of RE^{3+} cations in CeO_2 generally results in a lattice expansion with an increase in the average ionic radius. This is due to the larger ionic radius of La^{3+} (1.1 Å), Pr^{3+} (1.06 Å), Nd^{3+} (1.05 Å), and Dy^{3+} (0.97 Å) relative to Ce^{4+} (0.92 Å) in VII-fold coordination.[25−27] It is noted that Ce^{3+} in VII-fold coordination has a larger ionic radius (1.07 Å) relative to Ce^{4+}. As a noted exception to the trend, Tb inclusion does not increase the lattice volume of the fluorite structure. Tb^{4+} has ionic radii of 0.76 Å in VI-fold coordination and 0.88 Å in VIII-fold coordination, while Tb^{3+} has an ionic radius of 0.98 Å in VII-fold coordination. The valence states of the fluorite cations are discussed in further detail in connection with XPS results. Interestingly, samples containing RE cations display a clear decrease in the average crystallite size refined via XRD analysis (<10 nm crystalline correlation length) relative to CeO_2 (~20 nm). The average crystalline correlation lengths are found to be much smaller than the external particle morphologies discussed in the following section, revealing that the particles are highly disordered and/or contain many nanosized grains. It is noted that substitution of Ce^{4+} with larger (or smaller) RE cations is expected to induce lattice disorder, and fluorite compositions incorporating larger RE cations (La, Pr, and Nd) generally display more peak broadening (less crystallinity) than those incorporating smaller RE cations (Tb and Dy) in our series. High lattice disorder is additionally suggested by several large refined atomic displacement parameters in the reported Rietveld refinement results in Table 1.

The effectiveness of a catalyst is largely dependent on the accessible SA, which can be determined through the examination of the particle morphology. SEM was used to study the morphology of the fluorite sample series; all samples were found to be highly heterogeneous with a diverse range of particle sizes. In particular, micrometer scale porous flakes and spherical nanoparticle agglomerates are distinctly displayed, as shown by representative SEM images of $Nd_2Ce_2O_7$ in Figure S1a,b. Similar observations of the coexistence of micrometer sized flakes and spherical nanoparticles were reported in fluorite structured materials made via a solution combustion method by Cong et al.[28] SA values for the sample series measured using BET are displayed in Table 1, ranging between ~50 and ~90 m^2 g^{-1} across the series. The higher attained SAs at 600 °C of RE-containing samples may be related to higher

https://doi.org/10.1021/acsami.3c14977
ACS Appl. Mater. Interfaces 2024, 16, 7014−7025

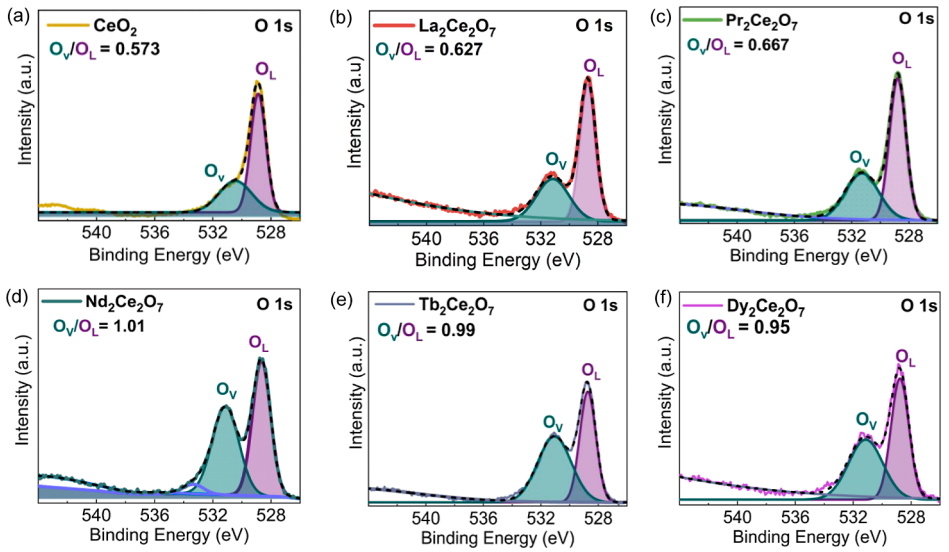

Figure 2. O 1s core level binding energy spectra of (a) CeO_2; (b) $La_2Ce_2O_7$; (c) $Pr_2Ce_2O_7$; (d) $Nd_2Ce_2O_7$; (e) $Tb_2Ce_2O_7$; and (f) $Dy_2Ce_2O_7$ catalysts. The area ratios of vacancy-related (O_V, green) and lattice-related (O_L, purple) components are provided.

decomposition temperatures of RE nitrates relative to Ce nitrate, leading to possible delayed nucleation and growth from solution.[29]

Energy-dispersive spectroscopy (EDS) measurements were performed on all RE^{3+}-containing samples to investigate the formation of a solid solution. Elemental mapping confirmed the homogeneous distribution of all elements present at the micron scale. Spectra were collected for various particle morphologies across sample locations to confirm that the different morphologies possess the same chemical composition and distribution. Representative EDS elemental mapping results for $Nd_2Ce_2O_7$ are shown in Figure S1c,d. Measured atomic ratios of RE cations to Ce from XRF measurements are displayed in Table S1 and were found to closely resemble the target stoichiometries with minor deviations.

XPS was used to determine the valence states of the elemental constituents present on the surface of the fluorite catalysts. As seen in Figure S2, the high-resolution Ce 3d spectra of CeO_2 show six peaks with multiplet splitting. The peaks were observed at 882.1, 888.4, and 897.9 eV for $3d_{5/2}$ and at 990.5, 906.8, and 916.3 eV for $3d_{3/2}$, confirming the presence of both Ce (III) and Ce (IV) commonly observed in ceria and ceria-based mixed oxides.[8,30,31]

The high-resolution La 3d spectrum of $La_2Ce_2O_7$ shown in Figure S3 displayed doublet splitting, which further deconvoluted into four peaks (two per doublet). The peaks observed at 834.5 and 851.4 eV correspond to the spin−orbit $3d_{5/2}$ and $3d_{3/2}$, respectively, while the peaks at 838.3 and 855.6 eV were identified as satellite peaks associated with $3d_{5/2}$ and $3d_{3/2}$, respectively.[32] These peaks represent La−O_x bonding, confirming the presence of La in the form of an oxide.[33]

Figure S4 shows the high-resolution Pr 3d spectrum of Pr in $Pr_2Ce_2O_7$ with two doublets at 932.8 and 953.4 eV and satellites at 928.4 and 984.2 eV, indicating the presence of the Pr(III) oxidation state. This observation aligns with the preferential trivalent state commonly observed for most RE ions.[34] Additionally, the satellites at lower binding energy are attributed to the $4f_3$ orbital, which has been shown to play a key role in the catalytic properties of RE-based oxides.[35,36]

The presence and bonding state of Nd in $Nd_2Ce_2O_7$ was confirmed from the high-resolution Nd 3d spectra shown in Figure S5b, which displayed two doublets at 977.8 and 982.3 eV, corresponding to a satellite and Nd(VI) of $3d_{5/2}$, as well as at 1000.1 and 1004.7 eV, corresponding to a satellite and Nd(III) of $3d_{3/2}$.[37,38] The 4d spectra (Figure S5c) exhibited 121.1 and 124.3 eV peaks, associated with a satellite and 4d in oxides.[39]

XPS analysis of $Tb_2Ce_2O_7$ from the high-resolution Tb 3d spectrum (Figure S6b) confirmed the presence of Tb(IV), as indicated by the observed characteristic doublet peaks of $3d_{5/2}$ and $3d_{3/2}$, along with their corresponding satellites at 1241.0, 1276.0, 1251.4, and 1287.0 eV, respectively. These results were consistent with the findings reported in the literature on RE oxides.[40,41]

As shown in Figure S7, the Dy 3d spectrum revealed doublet peaks corresponding to spin−orbit splitting at 1296.2 and 1334.6 eV for Dy(III) arising from $3d_{3/2}$ and $3d_{5/2}$, respectively.[42,43] Additionally, a satellite peak at 1303.9 eV was attributed to the Dy(IV) $3d_{5/2}$ components, indicating the presence of mixed Dy-ion states on the surfaces commonly seen in its oxides.[43]

The presence of oxygen vacancies in oxide-based electrocatalysts can strongly influence the kinetics of the OER by affecting the binding strengths of oxygen-containing intermediates, such as MOOH* and MOH* [M = metal cation(s)] with the catalyst surface.[44] Thus, the concentration of oxygen vacancies in the fluorite catalysts was investigated by analyzing the high-resolution O 1s XPS spectra for all of the samples in the series. As seen in Figure 2, the O 1s XPS spectra for all catalysts were deconvoluted into two main peak components: oxygen vacancy (O_V) and lattice oxygen (O_L). The O_L binding peak at approximately 528.8 eV in the O 1s XPS spectra of each catalyst is associated with a typical metal−oxygen bond of the lattice oxygen.[45] The peak at 530.9 eV corresponds to loosely absorbed oxygen species associated with oxygen vacancies. The O_V peak at 531.5 eV was attributed to the presence of surface chemisorbed oxygen associated with defects (oxygen vacancies).[45,46]

The proportion of surface oxygen vacancies in the catalysts was estimated by calculating the ratio of the O_V/O_L peak areas, with higher ratios indicating a larger amount of surface oxygen vacancies.[34] All of the binary fluorite compositions exhibit an

https://doi.org/10.1021/acsami.3c14977
ACS Appl. Mater. Interfaces 2024, 16, 7014−7025

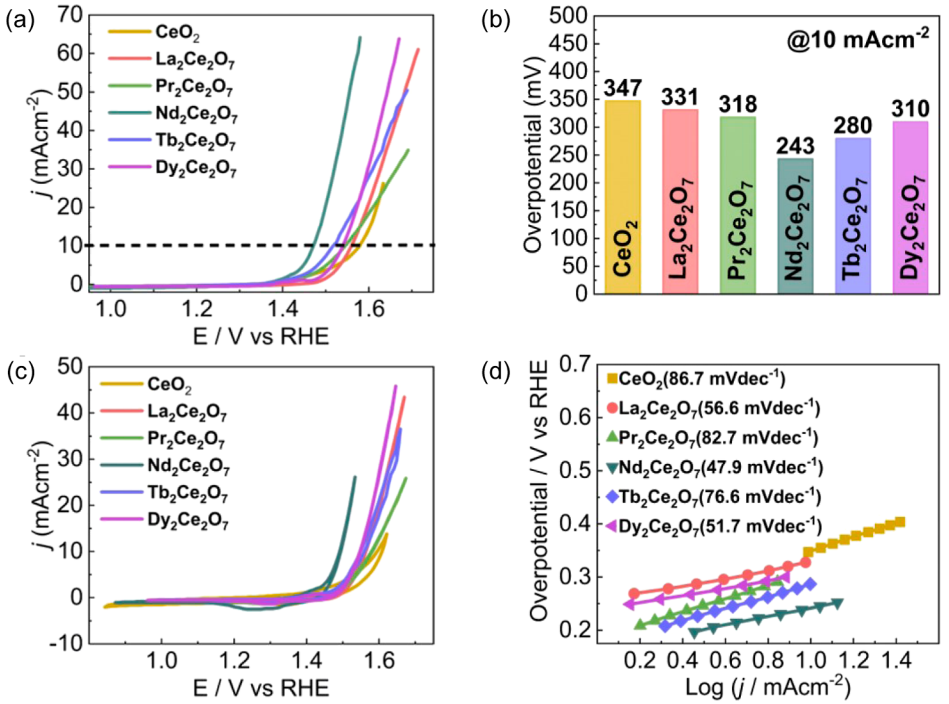

Figure 3. Electrocatalytic performance of CeO_2, $La_2Ce_2O_7$, $Pr_2Ce_2O_7$, $Nd_2Ce_2O_7$, $Tb_2Ce_2O_7$, and $Dy_2Ce_2O_7$ catalysts: (a) LSV curves; (b) overpotential at a current density of 10 mA cm^{-2}; (c) cyclic voltammograms; and (d) Tafel plots. All electrocatalysis data are measured in N_2-saturated 1 M KOH at a 10 mV s^{-1} scan rate.

increase in the oxygen vacancy concentration relative to CeO_2 to compensate for the extra positive charge introduced by substitution of Ce^{4+} with primarily RE^{3+} cations. Interestingly, $Nd_2Ce_2O_7$ displays the highest concentration of oxygen vacancies among all of the binary fluorites in the series. While Tb and Dy O_V/O_L values are close to that of Nd, they will likely have fewer overall charge compensating oxygen vacancies due to the incorporation of Tb^{4+} and, to a lesser extent, Dy^{4+}. These two factors suggest the potential for $Nd_2Ce_2O_7$ as an efficient electrocatalyst for the OER. Oxygen vacancies facilitate the adsorption of hydroxyl intermediates and initiate the reconstruction of defective surfaces under an applied potential,[32,47] resulting in improved OER performance. Achieving a high concentration of oxygen vacancies is crucial to enhancing the solid-to-charge carrier (STCH) performance, which is a key factor in determining electrochemical activity.[48]

Residual carbon was detected in the fluorite sample series via XPS. The C 1s spectra of all samples exhibit a sharp asymmetric peak at 285.0 eV, ascribed to amorphous carbon present in the form of C−C/C−H.[49] The peak at 288.8 eV is attributed to the incomplete oxidation of carbon species: O−C−O/O−C═O, which may arise from incomplete oxidation of the Pluronic P123 polymer used in the EISA synthesis process.[50] A similar concentration of the carbon residue was found to be present across all samples and is expected to increase the current density but not impact overpotential.

Electrocatalytic Performance for the OER. The electrocatalytic performance of the as-synthesized binary fluorites was assessed for the OER in a 1 M KOH alkaline solution using a three-electrode system. Linear sweep voltammetry (LSV) was employed to obtain OER polarization plots at a scan rate of 10 mV/s and compare the performance of the binary fluorite catalysts, as seen in Figure 3a.

As evidenced by the LSV curves, $Nd_2Ce_2O_7$ exhibited a significantly lower overpotential of 243 mV at a current density of 10 mA cm^{-2}, indicating higher catalytic activity than that of $La_2Ce_2O_7$ (overpotential of 331 mV), $Pr_2Ce_2O_7$ (overpotential of 318 mV), $Tb_2Ce_2O_7$ (overpotential of 280 mV), $Dy_2Ce_2O_7$ (overpotential of 310 mV), and CeO_2 (overpotential of 347 mV) (Figure 3b). The intrinsic catalytic activity of the catalysts ranging from the highest to the lowest can be ranked as follows: $Nd_2Ce_2O_7$ > $Tb_2Ce_2O_7$ > $Dy_2Ce_2O_7$ > $Pr_2Ce_2O_7$ > $La_2Ce_2O_7$ > CeO_2, suggesting that $Nd_2Ce_2O_7$ has the highest activity in the series. Notably, the CeO_2 catalyst, synthesized using a soft templating approach in this study, demonstrated an overpotential of 347 mV, surpassing other reported neat CeO_2 OER electrocatalysts in the literature.[6,51,52] This suggests that soft templating via EISA is a promising method for the synthesis of efficient electrocatalysts for the OER. Furthermore, all binary fluorite compositions exhibit an overpotential lower than that of CeO_2, presumably due to the increase in oxygen vacancy concentration, enhanced oxygen mobility from lattice disorder or expansion effects, and electronic perturbation effects resulting from RE cation incorporation into the fluorite lattice.

CV of all samples revealed preoxidation peaks associated with the oxidation of the active metal site (Figure 3c). The preoxidation peaks for $Nd_2Ce_2O_7$, $Tb_2Ce_2O_7$, $Dy_2Ce_2O_7$, $Pr_2Ce_2O_7$, $La_2Ce_2O_7$, and CeO_2 occurred at 1.35, 1.43, 1.39, 1.40, and 1.38 V vs RHE, respectively, at a scan rate of 10 mV s^{-1}, primarily originating from the contributions of Ce(III)/Ce(IV). This effect becomes more pronounced when varying the scan rates. The shift in the oxidation peak potential relative to the parent CeO_2 indicates the influence of electronic perturbation resulting from incorporating an RE element in the binary fluorites. Tafel plots derived from LSV curves were used to analyze the OER kinetics of the electrocatalyst. As shown in

https://doi.org/10.1021/acsami.3c14977
ACS Appl. Mater. Interfaces 2024, 16, 7014−7025

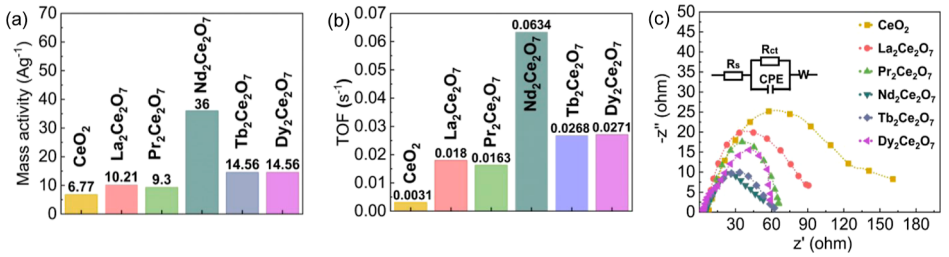

Figure 4. Electrocatalytic performance of CeO_2 (mustard), $La_2Ce_2O_7$ (pink), $Pr_2Ce_2O_7$ (green), $Nd_2Ce_2O_7$ (blue-green), $Tb_2Ce_2O_7$ (blue), and $Dy_2Ce_2O_7$ (violet) catalysts: (a) mass activity of different catalysts; (b) TOF; and (c) Nyquist plots in the AC frequency range between 100 kHz and 0.1 Hz at 0.45 V.

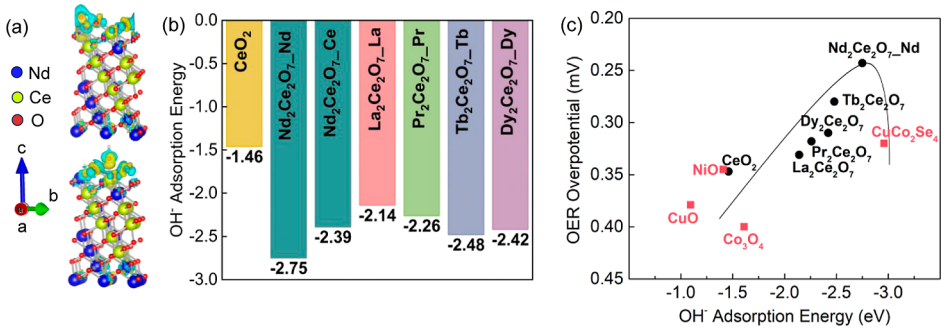

Figure 5. (a) Slab models of the (100) surface of $Nd_2Ce_2O_7$ used to calculate differential charge densities of adsorbed OH on Nd (top) and Ce (bottom) sites; (b) OH adsorption energy of the fluorite sample series calculated using the DFT VASP package; and (c) OER volcano plot comparing the fluorite electrocatalysts in this work (black circles) with transition metal-based electrocatalysts reported in the literature (red squares).[58,59]

Figure 3d, $Nd_2Ce_2O_7$ exhibited the smallest Tafel slope of 43.1 mV dec^{-1}, indicating faster electrocatalytic kinetics for the OER. Interestingly, the Tafel slopes for $Dy_2Ce_2O_7$ (51.7 mV dec^{-1}) and $La_2Ce_2O_7$ (56.6 mV dec^{-1}) were observed to be smaller than that of $Tb_2Ce_2O_7$ (76.6 mV dec^{-1}). Although $Tb_2Ce_2O_7$ is more catalytically active, it has electrokinetics slower than those of $Dy_2Ce_2O_7$ and $La_2Ce_2O_7$. Therefore, the electrokinetic activity of the fluorite series, as determined by the Tafel slope, follows the order $Nd_2Ce_2O_7$ (47.9 mV dec^{-1}) > $Dy_2Ce_2O_7$ (51.7 mV dec^{-1}) > $La_2Ce_2O_7$ (56.6 mV dec^{-1}) > $Tb_2Ce_2O_7$ (76.6 mV dec^{-1}) > $Pr_2Ce_2O_7$ (82.2 mV dec^{-1}) > CeO_2 (86.7 mV dec^{-1}). Importantly, a 50% RE cation substitution for Ce in the CeO_2 fluorite lattice enhances the electrokinetics of the OER, in addition to the activity. The binary fluorites reported in this study display improved OER performance compared to previously reported CeO_2-based electrocatalysts.[6,8,52−56]

To further evaluate the catalytic performance for the OER, the mass activities and TOF at an overpotential of 350 mV were calculated, as presented in Figure 4a,b respectively. Among all fluorite catalysts, $Nd_2Ce_2O_7$ demonstrated the highest OER activity, exhibiting a mass activity of 36.0 A g^{-1} and a TOF of 0.0643 s^{-1}. $Tb_2Ce_2O_7$ and $Dy_2Ce_2O_7$ showed very similar performances with the same mass activity of 14.56 A g^{-1} and TOF values of 0.0268 and 0.0271 s^{-1}, respectively. The superior OER activity of the $Nd_2Ce_2O_7$ catalyst can be tentatively attributed to the electronic structure perturbation resulting from the incorporation of Nd and an increased number of catalytically active sites originating from the higher concentration of oxygen vacancies.[57]

EIS analysis revealed that the electrical resistivity influences the OER activity. EIS spectra of the fluorite series revealed semicircular curves, indicating a combination of electron transfer and double-layer charging processes. The Nyquist plots generated at 0.45 V vs RHE are shown in Figure 4c. An equivalent circuit, shown in the inset in Figure 4c, consisting of the electrolyte resistance (R_s), charge transfer resistance (R_{ct}), constant phase element, and Warburg element (W) was used for evaluation (Table S2). $Nd_2Ce_2O_7$ exhibited the lowest R_{ct} of 7.95 Ω at a potential of 1.45 V vs RHE, followed by $Tb_2Ce_2O_7$ with an R_{ct} of 10.10 Ω. CeO_2 displayed the largest resistance of 18.1 Ω. A lower R_{ct} indicates faster charge transfer kinetics between the electrocatalyst surface and the electrolyte solution during the OER. The observed trend in the R_{ct} of the fluorite samples aligns with the trend observed in overpotential.

To elucidate differences in the charge density of adsorbed OH across the fluorite sample series, DFT calculations were performed. Slab models of the (100) crystal facet of the fluorites were constructed as shown by the representative crystal structure of $Nd_2Ce_2O_7$ in Figures 5a and S8, and the differential charge densities of the adsorbed OH group on the RE cation sites were calculated as seen in Figure 5b. For $Nd_2Ce_2O_7$, OH^- adsorption energy was calculated based on the RE and Ce sites, while only the RE cation site was used for calculations of the other samples in the fluorite series. According to the integrated charge density difference, the Nd/Ce−OH layer is surrounded by an apparent electron accumulation at Nd or Ce atoms (sky-blue region) and an electron reduction at the O atoms (yellow region), leading to new electronic states at the Nd/Ce−OH heterointerface. The largest electron cloud, depicted in Figure 5a, indicates a high rate of electron transfer and robust contact between OH* and the Nd on the catalyst surface; this is supported by the value of the adsorption energy of OH^- on Nd in $Nd_2Ce_2O_7$, which is negative (−2.68 eV) and has the smallest OH^- adsorption

https://doi.org/10.1021/acsami.3c14977
ACS Appl. Mater. Interfaces 2024, 16, 7014−7025

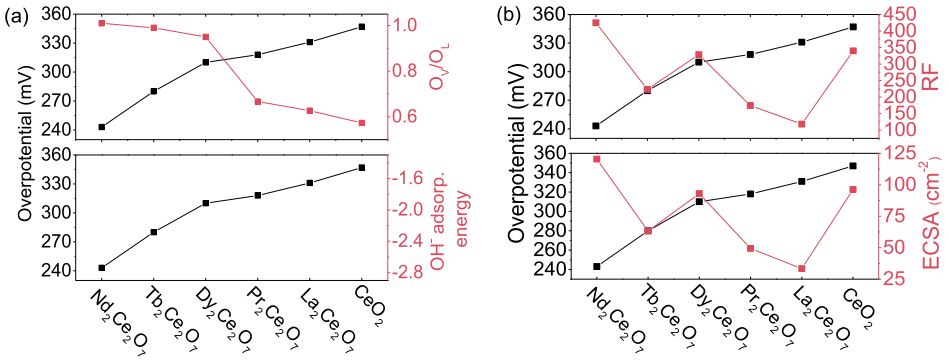

Figure 6. Comparison of the trends in overpotential versus (a) top: area ratios of vacancy-related (O_V) and lattice-related (O_L) oxygen calculated from the O 1s core level binding spectra from XPS measurements and bottom: OH^- adsorption from DFT calculations; (b) top: RF and bottom: ECSA for the fluorite sample series.

energy among all the fluorites investigated in this study. The smallest OH^- adsorption energy of $Nd_2Ce_2O_7$ accelerates the kinetics of the OER. It is noted that all $RE_2Ce_2O_7$ compositions studied here had a smaller OH^- adsorption energy relative to the CeO_2 surface. Qualitatively, the trend in smaller adsorption energies matches the trend in smaller overpotentials for the OER in the series.

Visualization of the relationship between OH^- adsorption energy and overpotential in the fluorite samples series is depicted in the form of a volcano plot, as shown in Figure 5c. OH^- adsorption is an exothermic process, and hence, higher OH^- adsorption (more negative energy) is associated with improved catalytic activity at the surface. However, very high negative OH^- adsorption leads to catalyst poisoning. Optimal OH^- adsorption energy (negative) yields the lowest overpotential and is located at the peak of the volcano plot. In the fluorite sample series, RE substitution leads to favorable OH^- adsorption on the catalyst site (more negative and more exothermic), decreasing overpotential. The trends in OER overpotential of the fluorite series and their corresponding OH^- adsorption from DFT calculations and the ratio of the O_V/O_L peak areas from the O 1s XPS spectra are shown in Figure 6a.

We observe a clear trend, suggesting that an increase in the concentration of oxygen vacancies leads to a decrease in the OH^- adsorption energy and a lower overpotential. An increase in the concentration of oxygen vacancies leads to more favorable OH^- adsorption (more exothermic process), leading to a lowering of overpotential. Surface-enriched oxygen vacancies play a key role in accommodating hydroxyls, enhancing the preoxidation of low oxidation species and facilitating the deprotonation/reconstruction of intermediates.[9] Additionally, achieving a higher valence state via coordination expansion is crucial in forming the initial active M-OOH* species for the OER.[60] The exposed RE sites exhibit improved electrophilicity and hydroxyl adsorption onto the Ce-active sites can be facilitated by oxygen vacancies (O_V), leading to adsorbed M-OH* intermediate species. Subsequently, this process triggers the deprotonation step at a minimal potential, forming active oxygen species (RE-OOH*) on the catalyst surface. This rationalizes the observed enhancement in the OER activity across the fluorite series. Importantly, many of the RE-based electrocatalysts in this work exhibit a lower OER overpotential than transition metal-based catalysts reported in the literature.[58,59]

To determine the role of morphology in enhancing the OER performance of the fluorite series, trends in the ECSAs of the catalysts were plotted against the OER activity, as shown in Figure 6b. ECSAs were determined by evaluating the specific electrochemical double-layer capacitance (C_{dl}) through CV measurements at various scan rates (2.5−50 mV s^{-1}) (Figures S9−S14). A larger ECSA value also leads to a higher surface roughness (RF) (also presented in Figure 6b), which is another parameter that is examined and can affect the catalytic activity. $Nd_2Ce_2O_7$ was found to have the largest ECSA and RF, likely due to the highly nanocrystalline nature of the sample, in corroboration with the broad diffraction peaks observed by XRD. Although CeO_2 exhibits higher ECSA and RF than the other binary fluorites, it showed the lowest OER activity (highest overpotential). Generally, for highly active catalysts, such as $Nd_2Ce_2O_7$, the larger ECSA observed translates to more exposed electrochemically active sites, facilitating electrolyte infiltration and surface interaction with the active sites of the electrocatalyst.[61] This leads to a high OER activity without hindrance from mass transfer limitations in the electrolyte.[62] Overall, an increase in the ECSA and RF does not directly correlate with a decrease in overpotential across the fluorite series, suggesting that while morphology plays an important role in catalytic performance, the chemical composition of the catalysts in this series and the resulting effects on oxygen vacancies and OH^- adsorption energy are responsible for the observed trends in the OER activity.

To investigate the preoxidation behavior of the catalysts during the OER, CV was employed. The CV plots reveal that the preoxidation peak of the catalyst becomes more pronounced at higher scan rates (Figures S15−S20). $La_2Ce_2O_7$, $Nd_2Ce_2O_7$, and CeO_2 demonstrated one reduction and one oxidation peak at all scan rates. Their oxidation peak shifts slightly toward a higher potential and their reduction peak toward a lower potential with the increasing scan rate. This indicates that they have similar redox processes (involving Ce). In contrast, $Pr_2Ce_2O_7$ and $Tb_2Ce_2O_7$ show two distinct reduction peaks and two overlapping oxidation peaks, with the reduction peaks more obviously identified, as shown in Figures S17 and S19, suggesting that both Ce in combination with Pr/Tb are involved in a unique redox process for these binary fluorite systems. Similarly, $Dy_2Ce_2O_7$ shows two overlapping reductions and two distinct oxidation peaks, where the oxidation peaks are more obviously recognized, as shown in Figure S20. Similarly, this suggests that Ce and Dy are both involved in this composition's preoxidation process. Overall,

https://doi.org/10.1021/acsami.3c14977
ACS Appl. Mater. Interfaces 2024, 16, 7014−7025

Table 2. Electrochemical Parameters for the Fluorite Sample Series

	CeO_2	$La_2Ce_2O_7$	$Pr_2Ce_2O_7$	$Nd_2Ce_2O_7$	$Tb_2Ce_2O_7$	$Dy_2Ce_2O_7$
onset potential (V)	1.52	1.49	1.47	1.42	1.44	1.48
overpotential@10 mA cm^{-2} (mV)	347	331	318	243	280	310
$Ce^{3+} \rightarrow Ce^{4+}$ oxidation peak potential (V)	1.38	1.43	1.41	1.35	1.39	1.4
TOF (s^{-1})	0.0031	0.018	0.0163	0.0634	0.0268	0.0271
mass activity (A g^{-1})	6.77	10.21	9.3	36	14.56	14.56
Tafel slope (mV dec^{-1})	86.7	56.6	82.2	47.9	76.6	51.7
ECSA (cm^2)	96.2	33.4	49.4	120.4	63.2	93
RF	339.8	118.1	174.3	425.5	223.2	328.6

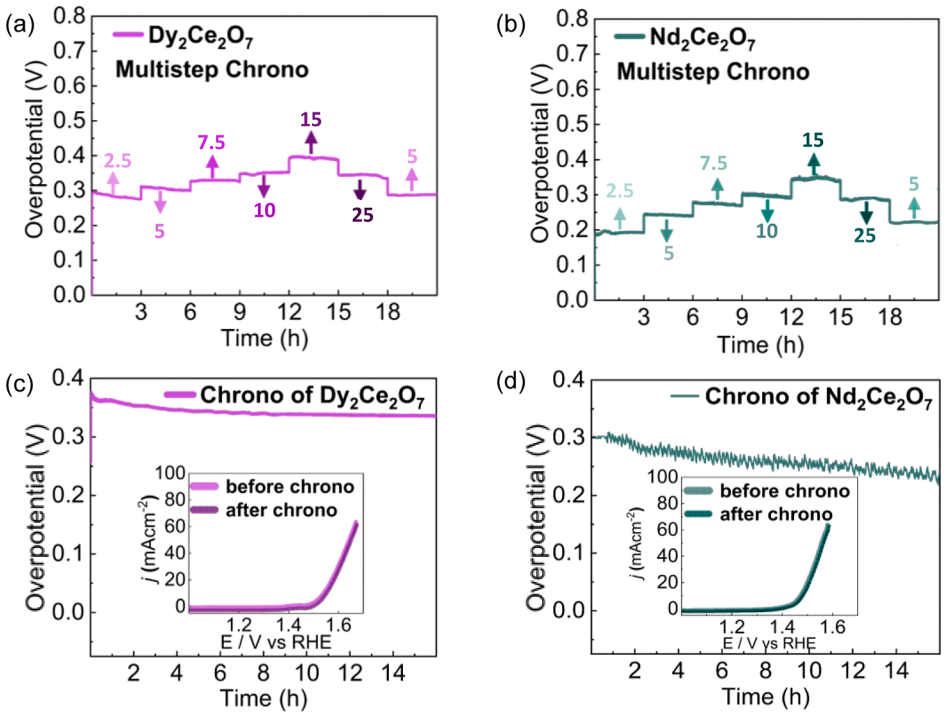

Figure 7. Multistep chronopotentiometry study at various current densities (mA cm^{-2}) for (a) $Dy_2Ce_2O_7$ and (b) $Nd_2Ce_2O_7$. Chronopotentiometry stability at a constant current density of 10 mA cm^{-2} for (c) $Dy_2Ce_2O_7$ and (d) $Nd_2Ce_2O_7$.

this indicates that Ce ions may serve as the main active site, while the other RE cations play differing roles in modulating the catalyst electronic and structural configuration, thereby significantly enhancing the electrocatalytic performance in the OER. The electrochemical parameters for the fluorite electrocatalysts are compared in Table 2.

OER Electrocatalytic Stability. The stabilities of the overall best performing catalyst ($Nd_2Ce_2O_7$) and the catalyst with the second highest electrokinetic activity, $Dy_2Ce_2O_7$, were evaluated by multistep chronopotentiometry at various currents ranging from 5 to 25 mA (Figure 7). The results demonstrate the remarkable stability of the fluorite series over extended periods and their ability to withstand varying currents without rapid degradation.

Additionally, the long-term durability of all the catalysts was investigated by subjecting them to constant potential measurements for 16 h (Figure S21). The fluorite electrocatalysts exhibited robust catalytic stability over 16 h under uninterrupted OER conditions at a constant current of 10 mA, as demonstrated by the long-term chronopotentiometry stability test (Figures 7 and S21). No significant deterioration or observable changes in the OER polarization plots of $Dy_2Ce_2O_7$ and $Nd_2Ce_2O_7$ were observed before and after the stability study, indicating excellent mass transfer properties and mechanical ruggedness of the electrode, as depicted in the inset of Figure 7c,d.

Additionally, XPS analysis (Figures S22−S27) reveals no notable alterations in the surface electronic states and elemental compositions of the catalysts before and after the stability measurements, indicating that the integrity of the catalysts remains intact. However, in the O 1s spectra of the fluorite samples, additional peaks are observed, indicating the adsorption of OH* species on the surface after activity. This suggests that OH^- adsorption occurs during catalyst activation and is attributed to physisorption. Furthermore, the C 1s spectra show additional peaks, where the peak at 295.6 eV is assigned to aromatic −C═O, while the peaks at 292.9 and 291.5 eV are attributed to an aromatic shakeup,[63] and the peak at 283.9 eV corresponds to sp^2 and sp^3-hybridized carbon (C═C/C−C).[64] The new carbon species observed post-OER arise from surface contamination and oxidation products resulting from the reaction, as previously described in the literature.[49] Overall, fluorite catalysts synthesized by using the EISA approach are found to have decent stability, with no apparent signs of degradation, indicating their promise to

https://doi.org/10.1021/acsami.3c14977
ACS Appl. Mater. Interfaces 2024, 16, 7014−7025

deliver the robustness and longevity needed for the use in OER applications.

The remarkable catalytic performance of the $Nd_2Ce_2O_7$ catalyst can primarily be attributed to an enhanced concentration of oxygen vacancies, which play a key role in accommodating hydroxyls and improving the electrokinetics of the OER process. In general, incorporating the RE element within the CeO_2 structure provides a favorable modification of the electronic structure and leads to improvements in the OER activity. Furthermore, the porous, nanostructured nature of the catalyst plays a significant role in minimizing the contact region between bubbles and the electrode, facilitating efficient bubble release and reactant transfer. The high SA to volume ratio of the nanocatalyst and the lattice expansion resulting from incorporating Nd increase the number of active sites and enhance the electron transport conductivity from the catalyst's surface. It will be of great interest to explore whether there is an optimal substitution level of Nd for Ce in the $Nd_xCe_{1-x}O_{2-\delta}$ solid solution series and whether incorporation of multiple REs in $RE_xCe_{1-x}O_{2-\delta}$ fluorites will further enhance the activity or stability for the OER electrocatalysis.

CONCLUSIONS

In this work, EISA was demonstrated as a promising, inexpensive, and scalable route to synthesize OER catalysts with a high SA and mesoporosity, belonging to the cerate fluorite class of materials. Although CeO_2 in this study appeared to have the highest overpotential and, consequently, the least activity toward the OER, its activity is higher than that of the pristine CeO_2 systems reported in the literature.

The substitution of 50% RE cations for Ce in the host CeO_2 fluorite lattice was found to significantly enhance the OER activity in a 1 M KOH electrolyte solution. Furthermore, all binary fluorite compositions demonstrate stability in an alkaline medium over long periods of operation at a constant potential. The improvement in the OER activity of the RE-containing binary fluorite compositions is ascribed to an increase in oxygen vacancies, which lowers the adsorption energy of the OH^- intermediate in the OER and thus lowers the OER overpotential.

Among the RE binary fluorite samples investigated, $Nd_2Ce_2O_7$ demonstrated the highest OER activity, exhibiting a low overpotential of 243 mV at a current density of 10 mA cm^{-2} with a low Tafel slope of 47.9 mV dec^{-1}, a high TOF of 0.0634 s^{-1}, and a high mass activity of 36 A g^{-1}. Additionally, $Nd_2Ce_2O_7$ displayed long-term durability in an alkaline medium. This superior OER activity can be attributed to the electronic redistribution, introduction of a large concentration of oxygen vacancies, and low OH^- adsorption energy induced by incorporating Nd cations into the CeO_2 host fluorite lattice. This study provides valuable insights into using RE element substitution to tailor the structure and electronic properties of the fluorite class of materials, enabling the development of highly active and stable electrocatalysts. Importantly, we demonstrate that RE oxide OER catalysts with high activity and stability can be achieved using the low-cost EISA synthesis route, without the incorporation of transition and noble metals.

ASSOCIATED CONTENT

Supporting Information

The Supporting Information is available free of charge at https://pubs.acs.org/doi/10.1021/acsami.3c14977.

Representative SEM and EDS images of $Nd_2Ce_2O_7$ synthesized at 600 °C using EISA; XRF measurements of the fluorite sample series; table of equivalent circuit parameters from fitting of EIS experimental data; XPS spectra of the fluorite series before and after the OER; representative crystal structure models of $Nd_2Ce_2O_7$ used to perform DFT calculations; CV curves of the fluorite series measured at different scan rates; and chronopotentiometry stability of the fluorite series, with LSV curves shown before and after the OER (PDF)

AUTHOR INFORMATION

Corresponding Author

Katharine Page − *Department of Materials Science and Engineering, University of Tennessee, Knoxville, Tennessee 37996, United States; Neutron Scattering Division, Oak Ridge National Laboratory, Oak Ridge, Tennessee 37831, United States;* orcid.org/0000-0002-9071-3383; Email: kpage10@utk.edu

Authors

Sreya Paladugu − *Department of Materials Science and Engineering, University of Tennessee, Knoxville, Tennessee 37996, United States*

Ibrahim Munkaila Abdullahi − *Department of Chemistry, Missouri University of Science and Technology, Rolla, Missouri 65409, United States*

Harish Singh − *Department of Chemistry, Missouri University of Science and Technology, Rolla, Missouri 65409, United States*

Sam Spinuzzi − *Department of Chemistry, Missouri University of Science and Technology, Rolla, Missouri 65409, United States*

Manashi Nath − *Department of Chemistry, Missouri University of Science and Technology, Rolla, Missouri 65409, United States;* orcid.org/0000-0002-5058-5313

Complete contact information is available at: https://pubs.acs.org/10.1021/acsami.3c14977

Notes

The authors declare no competing financial interest.

ACKNOWLEDGMENTS

This synthesis efforts in this work were supported by the donors of the American Chemical Society Petroleum Research Fund for support of the materials synthesis efforts in this research. This work was supported by the donors of ACS Petroleum Research Fund under Grant PRF# 62728-DNI3. XRD measurements were completed at the Diffraction Facility at the Institute for Advanced Materials and Manufacturing at the University of Tennessee, Knoxville. DFT calculations were performed at the Molecular Foundry under proposal no. 7804 in collaboration with David Prendergast.

REFERENCES

(1) Song, X. Z.; Zhu, W. Y.; Wang, X. F.; Tan, Z. Recent Advances of CeO_2-Based Electrocatalysts for Oxygen and Hydrogen Evolution as well as Nitrogen Reduction. *ChemElectroChem* **2021**, *8*, 996−1020.

(2) Li, Q.; Song, L.; Liang, Z.; Sun, M.; Wu, T.; Huang, B.; Luo, F.; Du, Y.; Yan, C.-H. A Review on CeO_2-Based Electrocatalyst and Photocatalyst in Energy Conversion. *Adv. Energy Sustainability Res.* **2021**, *2*, 2000063.

(3) Bucci, A.; García-Tecedor, M.; Corby, S.; Rao, R. R.; Martin-Diaconescu, V.; Oropeza, F. E.; de la Peña O'Shea, V. A.; Durrant, J. R.; Giménez, S.; Lloret-Fillol, J. Self-supported ultra-active NiO-based electrocatalysts for the oxygen evolution reaction by solution combustion. *J. Mater. Chem. A* **2021**, *9*, 12700−12710.
(4) Suen, N.-T.; Hung, S.-F.; Quan, Q.; Zhang, N.; Xu, Y.-J.; Chen, H. M. Electrocatalysis for the oxygen evolution reaction: recent development and future perspectives. *Chem. Soc. Rev.* **2017**, *46*, 337−365.
(5) Park, S.; Shao, Y.; Liu, J.; Wang, Y. Oxygen electrocatalysts for water electrolyzers and reversible fuel cells: status and perspective. *Energy Environ. Sci.* **2012**, *5*, 9331−9344.
(6) Ghosh, D.; Manikanta Kumar, M.; Raj, C. R.; Pradhan, D. Bifunctional Catalytic Activity of Solvothermally Synthesized CeO_2 Nanosphere/NiO Nanoflake Nanocomposites. *ACS Appl. Energy Mater.* **2022**, *5*, 5666−5679.
(7) Yu, J.; Cao, Q.; Li, Y.; Long, X.; Yang, S.; Clark, J. K.; Nakabayashi, M.; Shibata, N.; Delaunay, J.-J. Defect-Rich $NiCeO_x$ Electrocatalyst with Ultrahigh Stability and Low Overpotential for Water Oxidation. *ACS Catal.* **2019**, *9*, 1605−1611.
(8) Qiu, B.; Wang, C.; Zhang, N.; Cai, L.; Xiong, Y.; Chai, Y. CeO_2-Induced Interfacial Co^{2+} Octahedral Sites and Oxygen Vacancies for Water Oxidation. *ACS Catal.* **2019**, *9*, 6484−6490.
(9) Xiao, Z.; Huang, Y. C.; Dong, C. L.; Xie, C.; Liu, Z.; Du, S.; Chen, W.; Yan, D.; Tao, L.; Shu, Z.; et al. Operando Identification of the Dynamic Behavior of Oxygen Vacancy-Rich Co_3O_4 for Oxygen Evolution Reaction. *J. Am. Chem. Soc.* **2020**, *142*, 12087−12095.
(10) Song, F.; Bai, L.; Moysiadou, A.; Lee, S.; Hu, C.; Liardet, L.; Hu, X. Transition Metal Oxides as Electrocatalysts for the Oxygen Evolution Reaction in Alkaline Solutions: An Application-Inspired Renaissance. *J. Am. Chem. Soc.* **2018**, *140*, 7748−7759.
(11) Coduri, M.; Checchia, S.; Longhi, M.; Ceresoli, D.; Scavini, M. Rare Earth Doped Ceria: The Complex Connection Between Structure and Properties. *Front. Chem.* **2018**, *6*, 526.
(12) Aarthi, U.; Shukla, D.; Rengaraj, S.; Babu, K. S. Ordered to defect fluorite structural transition in $Ce_{1-x}Nd_xO_{2-\delta}$ system and its influence on ionic conductivity. *J. Alloys Compd.* **2020**, *838*, 155534.
(13) Mamontov, E.; Egami, T.; Brezny, R.; Koranne, M.; Tyagi, S. Lattice defects and oxygen storage capacity of nanocrystalline ceria and ceria-zirconia. *J. Phys. Chem. B* **2000**, *104*, 11110−11116.
(14) Duan, C.; Li, X.; Wang, D.; Wang, Z.; Sun, H.; Zheng, R.; Liu, Y. Nanosized high entropy spinel oxide $(FeCoNiCrMn)_3O_4$ as a highly active and ultra-stable electrocatalyst for the oxygen evolution reaction. *Sustainable Energy Fuels* **2022**, *6*, 1479−1488.
(15) Sarma, S. C.; Subbarao, U.; Khulbe, Y.; Jana, R.; Peter, S. C. Are we underrating rare earths as an electrocatalyst? The effect of their substitution in palladium nanoparticles enhances the activity towards ethanol oxidation reaction. *J. Mater. Chem. A* **2017**, *5*, 23369−23381.
(16) Li, C.; Wang, P.; He, M.; Yuan, X.; Fang, Z.; Li, Z. Rare earth-based nanomaterials in electrocatalysis. *Coord. Chem. Rev.* **2023**, *489*, 215204.
(17) Chen, H.; Liang, X.; Liu, Y.; Ai, X.; Asefa, T.; Zou, X. Active Site Engineering in Porous Electrocatalysts. *Adv. Mater.* **2020**, *32*, 2002435.
(18) Qi, J.; Zhang, W.; Cao, R. Porous Materials as Highly Efficient Electrocatalysts for the Oxygen Evolution Reaction. *ChemCatChem* **2018**, *10*, 1206−1220.
(19) Dantelle, G.; Beauquis, S.; Le Dantec, R.; Monnier, V.; Galez, C.; Mugnier, Y. Solution-Based Synthesis Routes for the Preparation of Noncentrosymmetric 0-D Oxide Nanocrystals with Perovskite and Nonperovskite Structures. *Small* **2022**, *18*, 2200992.
(20) Gonçalves, A. A. S.; Jaroniec, M. Evaporation-induced self-assembly synthesis of nanostructured alumina-based mixed metal oxides with tailored porosity. *J. Colloid Interface Sci.* **2019**, *537*, 725−735.
(21) Coelho, A. A. *TOPAS* and *TOPAS-Academic*: an optimization program integrating computer algebra and crystallographic objects written in C++. *J. Appl. Crystallogr.* **2018**, *51*, 210−218.
(22) McCrory, C. C. L.; Jung, S.; Peters, J. C.; Jaramillo, T. F. Benchmarking Heterogeneous Electrocatalysts for the Oxygen Evolution Reaction. *J. Am. Chem. Soc.* **2013**, *135*, 16977−16987.
(23) Abdullahi, I. M.; Nath, M. Molecular Cluster Complex of High-Valence Chromium Selenide Carbonyl as Effective Electrocatalyst for Water Oxidation. *Catalysts* **2023**, *13*, 721.
(24) Schmitt, R.; Nenning, A.; Kraynis, O.; Korobko, R.; Frenkel, A. I.; Lubomirsky, I.; Haile, S. M.; Rupp, J. L. A review of defect structure and chemistry in ceria and its solid solutions. *Chem. Soc. Rev.* **2020**, *49*, 554−592.
(25) Shannon, R. D.; Prewitt, C. T. Effective ionic radii in oxides and fluorides. *Acta Crystallogr., Sect. B: Struct. Sci., Cryst. Eng. Mater.* **1969**, *25*, 925−946.
(26) Shannon, R. D. Revised effective ionic radii and systematic studies of interatomic distances in halides and chalcogenides. *Acta Crystallogr., Sect. A: Found. Adv.* **1976**, *32*, 751−767.
(27) Bryan, R. F. Fundamentals of crystallography. IUCr Texts on Crystallography No. 2 by C. Giacovazzo, H. L. Monaco, D. Viterbo, F. Scordari, G. Gilli, G. Zanotti and M. Catti. *Acta Crystallogr., Sect. A: Found. Adv.* **1993**, *49*, 373−374.
(28) Cong, L.; Zhang, S.; Gu, S.; Li, W. Thermophysical properties of a novel high entropy hafnate ceramic. *J. Mater. Sci. Technol.* **2021**, *85*, 152−157.
(29) Cochran, E. A.; Woods, K. N.; Johnson, D. W.; Page, C. J.; Boettcher, S. W. Unique chemistries of metal-nitrate precursors to form metal-oxide thin films from solution: Materials for electronic and energy applications. *J. Mater. Chem. A* **2019**, *7*, 24124−24149.
(30) Maslakov, K. I.; Teterin, Y. A.; Popel, A. J.; Teterin, A. Y.; Ivanov, K. E.; Kalmykov, S. N.; Petrov, V. G.; Petrov, P. K.; Farnan, I. XPS study of ion irradiated and unirradiated CeO_2 bulk and thin film samples. *Appl. Surf. Sci.* **2018**, *448*, 154−162.
(31) Zhu, Y.; Jain, N.; Hudait, M.; Maurya, D.; Varghese, R.; Priya, S. X-ray photoelectron spectroscopy analysis and band offset determination of CeO_2 deposited on epitaxial (100), (110), and (111) Ge. *J. Vac. Sci. Technol., B: Microelectron. Nanometer Struct.–Process., Meas., Phenom.* **2014**, *32*, 011217.
(32) Nguyen, T. X.; Liao, Y.-C.; Lin, C.-C.; Su, Y.-H.; Ting, J.-M. Advanced High Entropy Perovskite Oxide Electrocatalyst for Oxygen Evolution Reaction. *Adv. Funct. Mater.* **2021**, *31*, 2101632.
(33) Nundy, S.; Tatar, D.; Kojčinović, J.; Ullah, H.; Ghosh, A.; Mallick, T.; Meinusch, R.; Smarsly, B.; Tahir, A.; Djerdj, I. Bandgap Engineering in Novel Fluorite-Type Rare Earth High-Entropy Oxides (RE-HEOs) with Computational and Experimental Validation for Photocatalytic Water Splitting Applications. *Adv. Sustainable Syst.* **2022**, *6*, 2200067.
(34) Zhao, J.; Liu, C.; Li, J.; Wu, R.; Wang, J.; Qian, H.; Guo, H.; Li, J.; Ibrahim, K. Oxygen vacancy induced electronic structure variation in the $La_{0.2}Sr_{0.8}MnO_3$ thin film. *AIP Adv.* **2019**, *9*, 55208.
(35) Aragón, F. H.; Gonzalez, I.; Coaquira, J. A. H.; Hidalgo, P.; Brito, H. F.; Ardisson, J. D.; Macedo, W. A. A.; Morais, P. C. Structural and Surface Study of Praseodymium-Doped SnO_2 Nanoparticles Prepared by the Polymeric Precursor Method. *J. Phys. Chem. C* **2015**, *119*, 8711−8717.
(36) Koelling, D. D.; Boring, A. M.; Wood, J. H. The electronic structure of CeO_2 and PrO_2. *Solid State Commun.* **1983**, *47*, 227−232.
(37) Baltrus, J. P.; Keller, M. J. Rare earth oxides Eu_2O_3 and Nd_2O_3 analyzed by XPS. *Surf. Sci. Spectra* **2019**, *26*, 14001.
(38) Brunckova, H.; Kolev, H.; Kanuchova, M. X-ray photoelectron spectroscopy study of neodymium niobate and tantalate precursors and thin films. *Surf. Interface Anal.* **2019**, *51*, 326−335.
(39) Moulder, J. F.; Stickle, W. F.; Sobol, W. M.; Bomben, K. D. *Handbook of X-ray Photoelectron Spectroscopy*; Physical Electronics Division, Perkin-Elmer Corporation, 1992.
(40) Blanco, G.; Pintado, J. M.; Bernal, S.; Cauqui, M. A.; Corchado, M. P.; Galtayries, A.; Ghijsen, J.; Sporken, R.; Eickhoff, T.; Drube, W. Influence of the nature of the noble metal (Rh,Pt) on the low-temperature reducibility of a Ce/Tb mixed oxide with application as TWC component. *Surf. Interface Anal.* **2002**, *34*, 120−124.

https://doi.org/10.1021/acsami.3c14977
ACS Appl. Mater. Interfaces 2024, 16, 7014−7025

(41) Zhao, Y.; Li, J.-G.; Guo, M.; Yang, X. Structural and photoluminescent investigation of LTbH/LEuH nanosheets and their color-tunable colloidal hybrids. *J. Mater. Chem. C* **2013**, *1*, 3584−3592.
(42) Tangoulis, V.; Lalioti, N.; Parthenios, J.; Boukos, N.; Malina, O.; Tuček, J.; Zbořil, R. Noncovalent Grafting of a Dy^{III}_2 Single-Molecule Magnet onto Chemically Modified Multiwalled Carbon Nanotubes. *Inorg. Chem.* **2018**, *57*, 6391−6400.
(43) Gil, Y.; Gimeno-Muñoz, R.; Santana, R. C. d.; Aliaga-Alcalde, N.; Fuentealba, P.; Aravena, D.; González-Campo, A.; Spodine, E. Luminescence of Macrocyclic Mononuclear Dy^{III} Complexes and Their Immobilization on Functionalized Silicon-Based Surfaces. *Inorg. Chem.* **2022**, *61*, 16347−16355.
(44) Wang, X.; Zhong, H.; Xi, S.; Lee, W. S. V.; Xue, J. Understanding of Oxygen Redox in the Oxygen Evolution Reaction. *Adv. Mater.* **2022**, *34*, 2107956.
(45) Hua, B.; Zhang, Y.-Q.; Yan, N.; Li, M.; Sun, Y.-F.; Chen, J.; Li, J.; Luo, J.-L. The Excellence of Both Worlds: Developing Effective Double Perovskite Oxide Catalyst of Oxygen Reduction Reaction for Room and Elevated Temperature Applications. *Adv. Funct. Mater.* **2016**, *26*, 4106−4112.
(46) Tang, L.; Yang, Y.; Guo, H.; Wang, Y.; Wang, M.; Liu, Z.; Yang, G.; Fu, X.; Luo, Y.; Jiang, C.; Zhao, Y.; Shao, Z.; Sun, Y. High Configuration Entropy Activated Lattice Oxygen for O_2 Formation on Perovskite Electrocatalyst. *Adv. Funct. Mater.* **2022**, *32*, 2112157.
(47) Zhu, Y.; Zhou, W.; Yu, J.; Chen, Y.; Liu, M.; Shao, Z. Enhancing Electrocatalytic Activity of Perovskite Oxides by Tuning Cation Deficiency for Oxygen Reduction and Evolution Reactions. *Chem. Mater.* **2016**, *28*, 1691−1697.
(48) Pavone, M.; Ritzmann, A. M.; Carter, E. A. Quantum-mechanics-based design principles for solid oxide fuel cell cathode materials. *Energy Environ. Sci.* **2011**, *4*, 4933−4937.
(49) Lewin, E.; Persson, P.; Lattemann, M.; Stüber, M.; Gorgoi, M.; Sandell, A.; Ziebert, C.; Schäfers, F.; Braun, W.; Halbritter, J.; et al. On the origin of a third spectral component of C1s XPS-spectra for nc-TiC/a-C nanocomposite thin films. *Surf. Coat. Technol.* **2008**, *202*, 3563−3570.
(50) Li, J. P. H.; Zhou, X.; Pang, Y.; Zhu, L.; Vovk, E. I.; Cong, L.; van Bavel, A. P.; Li, S.; Yang, Y. Understanding of binding energy calibration in XPS of lanthanum oxide by in situ treatment. *Phys. Chem. Chem. Phys.* **2019**, *21*, 22351−22358.
(51) Gao, M.; Wang, Z.; Sun, S.; Jiang, D.; Chen, M. Interfacial engineering of CeO_2 on NiCoP nanoarrays for efficient electrocatalytic oxygen evolution. *Nanotechnology* **2021**, *32*, 195704.
(52) Xie, H.; Geng, Q.; Liu, X.; Mao, J. Interface engineering for enhancing electrocatalytic oxygen evolution reaction of CoS/CeO_2 heterostructures. *Front. Chem. Sci. Eng.* **2022**, *16*, 376−383.
(53) Zhang, H.; Du, J.; Niu, D.; Hu, S.; Zhang, X. Synthesis and Characterization of Fe^{3+} and CeO_2 Co-decorated NiOOH Electrocatalysts Supported by Nickel Foam for the Oxygen Evolution Reaction. *Int. J. Electrochem. Sci.* **2019**, *14*, 6532−6545.
(54) Li, T.; Li, S.; Liu, Q.; Tian, Y.; Zhang, Y.; Fu, G.; Tang, Y. Hollow Co_3O_4/CeO_2 Heterostructures in Situ Embedded in N-Doped Carbon Nanofibers Enable Outstanding Oxygen Evolution. *ACS Sustainable Chem. Eng.* **2019**, *7*, 17950−17957.
(55) Huang, J.; Sheng, H.; Ross, R. D.; Han, J.; Wang, X.; Song, B.; Jin, S. Modifying redox properties and local bonding of Co_3O_4 by CeO_2 enhances oxygen evolution catalysis in acid. *Nat. Commun.* **2021**, *12*, 3036.
(56) Li, Y.; Zhang, X.; Zheng, Z. CeO2 Functionalized Cobalt Layered Double Hydroxide for Efficient Catalytic Oxygen-Evolving Reaction. *Small* **2022**, *18*, 2107594.
(57) Wang, H.; Chen, X.; Huang, D.; Zhou, M.; Ding, D.; Luo, H. Cation Deficiency Tuning of $LaCoO_3$ Perovskite as Bifunctional Oxygen Electrocatalyst. *ChemCatChem* **2020**, *12*, 2768−2775.
(58) Cao, X.; Medvedeva, J. E.; Nath, M. Copper Cobalt Selenide as a High-Efficiency Bifunctional Electrocatalyst for Overall Water Splitting: Combined Experimental and Theoretical Study. *ACS Appl. Energy Mater.* **2020**, *3*, 3092−3103.
(59) Nath, M.; De Silva, U.; Singh, H.; Perkins, M.; Liyanage, W. P. R.; Umapathi, S.; Chakravarty, S.; Masud, J. Cobalt Telluride: A Highly Efficient Trifunctional Electrocatalyst for Water Splitting and Oxygen Reduction. *ACS Appl. Energy Mater.* **2021**, *4*, 8158−8174.
(60) Petitto, S. C.; Marsh, E. M.; Carson, G. A.; Langell, M. A. Cobalt oxide surface chemistry: The interaction of CoO(100), Co_3O_4(110) and Co_3O_4(111) with oxygen and water. *J. Mol. Catal. A: Chem.* **2008**, *281*, 49−58.
(61) Liu, K.; Zhu, Z.; Jiang, M.; Li, L.; Ding, L.; Li, M.; Sun, D.; Yang, G.; Fu, G.; Tang, Y. Boosting Electrocatalytic Oxygen Evolution over Ce−Co_9S_8 Core−Shell Nanoneedle Arrays by Electronic and Architectural Dual Engineering. *Chem.—Eur. J.* **2022**, *28*, No. e202200664.
(62) Wang, T.; Chen, H.; Yang, Z.; Liang, J.; Dai, S. High-Entropy Perovskite Fluorides: A New Platform for Oxygen Evolution Catalysis. *J. Am. Chem. Soc.* **2020**, *142*, 4550−4554.
(63) Gengenbach, T. R.; Major, G. H.; Linford, M. R.; Easton, C. D. Practical guides for x-ray photoelectron spectroscopy (XPS): Interpreting the carbon 1s spectrum. *J. Vac. Sci. Technol.* **2021**, *39*, 13204.
(64) Ranganathan, K.; Morais, A.; Nongwe, I.; Longo, C.; Nogueira, A. F.; Coville, N. J. Study of photoelectrochemical water splitting using composite films based on TiO_2 nanoparticles and nitrogen or boron doped hollow carbon spheres as photoanodes. *J. Mol. Catal. A: Chem.* **2016**, *422*, 165−174.

https://doi.org/10.1021/acsami.3c14977
ACS Appl. Mater. Interfaces 2024, 16, 7014−7025